








Laboratory observation of plasmoid-dominated magnetic reconnection in hybrid collisional-collisionless regime

Zhonghai Zhao ^{1,5}, Honghai An^{2,5}, Yu Xie¹, Zhu Lei¹, Weipeng Yao¹, Wenqiang Yuan ¹, Jun Xiong², Chen Wang ², Junjian Ye², Zhiyong Xie², Zhiheng Fang², Anle Lei², Wenbing Pei², Xiantu He³, Weimin Zhou ⁴✉, Wei Wang ²✉, Shaoping Zhu ³✉ & Bin Qiao ¹✉

Magnetic reconnection, breaking and reorganization of magnetic field topology, is a fundamental process for rapid release of magnetic energy into plasmas that occurs pervasively throughout the universe. In natural circumstances, the plasma properties on either side of the reconnection layer are almost asymmetric, in particular for the collision rates that critically determine the underlying reconnection mechanism. To date, all laboratory experiments on magnetic reconnections have been limited to purely collisional or collisionless regimes. Here, we report a well-designed experimental investigation on magnetic reconnections in a hybrid collisional-collisionless regime by interactions between laser-ablated copper and plastic plasmas. We directly observe the topology evolutions of the whole process of this asymmetric magnetic reconnection by highly-resolved proton radiography. Through this, we show that the growth rate of tearing instability in such a hybrid regime is still extremely large, resulting in rapid formation of multiple plasmoids and generation of plasmoid-dominated current sheet.

¹Center for Applied Physics and Technology, HEDPS, and SKLNPT, School of Physics, Peking University, Beijing 100871, China. ²Shanghai Institute of Laser Plasma, China Academy of Engineering Physics (CAEP), Shanghai 201800, China. ³Institute of Applied Physics and Computational Mathematics, Beijing 100094, China. ⁴Science and Technology on Plasma Physics Laboratory, Research Center of Laser Fusion, China Academy of Engineering Physics (CAEP), Mianyang 621900, China. ⁵These authors contributed equally: Zhonghai Zhao, Honghai An. ✉email: zhouwm@caep.cn; wei_wang@fudan.edu.cn; zsp@iapcm.ac.cn; bqiao@pku.edu.cn

Magnetic reconnection is a physical process occurring nearly anywhere there's plasma, in which the magnetic topology is rearranged and magnetic energy is converted to kinetic energy, thermal energy, and particle acceleration^{1,2}. As plasma makes up the stars and ninety-nine percent of the visible universe, magnetic reconnection is ubiquitous and plays a key role in many energetic events throughout the whole universe such as magnetospheric substorms, coronal mass ejection, solar flares³ and so on. However, due to the vastly different plasma properties and spatiotemporal scales, it is hard to give a universal model for describing the mechanism of magnetic reconnection.

A key element of magnetic reconnection is the reconnection electric field E_{rec} , which plays a pivotal role in both energy conversion and production of energetic particles by doing work on particles. The normalized reconnection electric field is also employed to represent the reconnection rate. Theoretical and simulation studies have shown that E_{rec} depends heavily on the plasma properties⁴, in particular, the collision rate as a combination of plasma density and temperature. In the strongly collisional regime, such as magnetic reconnections in solar/stellar photosphere and chromosphere⁵, E_{rec} is induced by the plasma resistivity as described by the Sweet-Parker model^{6,7}, which, however, leads to a rather slow reconnection with low reconnection rate. By contrast, in the weakly collisional or collisionless regime, such as those occurring in magnetopause⁸ and magnetotail⁹, E_{rec} is contributed mainly by the off-diagonal (nongyrotropic) component of the electron pressure tensor^{10,11}, resulting in a fast reconnection that is independent of the plasma collision rate.

However, for some natural circumstances in the universe, a large class of magnetic reconnection lies in a hybrid regime where the reconnection plasmas have asymmetric collision rates with one side in a strongly-collisional state and the other in a weakly-collisional or collisionless state. One of the most typical scenarios for such hybrid collisional-collisionless magnetic reconnection occurs in the solar/stellar atmosphere¹², see Fig. 1a, when the cool (electron temperature $T_e \sim 10^4$ K), dense (plasma density $n_e \sim 10^{11} \text{ cm}^{-3}$) filaments erupting from the chromosphere collide with the hot ($T_e \sim 10^6$ K), tenuous ($n_e \sim 10^8 \text{ cm}^{-3}$) loops in the corona, which has been directly observed by the Solar Dynamics Observatory (SDO)¹³. As we know, the collisional mean free path $\lambda_{ei} \propto T_e^2 n_e^{-1}$, therefore, the plasma in the filaments is highly collisional while that in the coronal loops is collisionless. Such hybrid magnetic reconnection may also occur when the magnetic

fields in the dense accretion disk collide with those in the tenuous interstellar medium.

So far, most laboratory experiments^{14–18} of magnetic reconnection are focused on the purely collisional and/or collisionless regimes, in particular, relativistic¹⁹ or electron-dominated²⁰ reconnection is almost always collisionless. The reconnection experiment^{21,22} by laser-driven colliding plasmas with asymmetric flow velocities arising from the delay between laser drives are carried out, where, however, almost no impacts on the reconnection dynamics have been observed because the reconnection plasmas are both still purely collisionless. Although the dynamic transition of reconnection from collisional to collisionless, through the current sheet thinning, has been discussed theoretically^{23,24}, the effect of asymmetry therein remains unclear. In addition, to date, the evolutions of magnetic topologies for the whole process of the plasmoid-dominated magnetic reconnections^{25,26} including the growth of tearing instabilities²⁷ and the formation of multiple plasmoids^{28,29} have never been directly observed, where only indirect measurements through the interferometry^{30,31} have been given.

Here, we report result of the first experiment, to the best of our knowledge, on asymmetric magnetic reconnections in the hybrid collisional-collisionless regime by colliding of laser-irradiated high-Z copper (Cu) and low-Z plastic (CH) plasmas. It shows that the growth rate of the tearing instability in such a hybrid regime is still extremely large, resulting in rapid formation of multiple plasmoids. Combined with numerical simulations, this rate is lower than that in the purely collisionless regime but much higher than the collisional case (where only single X-point forms). Using the temporally and spatially highly-resolved proton radiography, we provide the direct measurement of magnetic topology evolutions for the whole process of such plasmoid-dominated magnetic reconnection, so that the specific reconnection dynamics including growth of the tearing instability and formation of multiple plasmoids are well characterized. The experimental results are well reproduced and explained by self-consistently combining the radiation-magnetohydrodynamic (RMHD) and particle-in-cell (PIC) simulations as well as the proton radiography iterative inversion algorithm. Physically, in the hybrid magnetic reconnection, the reconnection electric field show much distinct feature, which is large and grows fast at the collisionless plasma side induced by the non-gyrotropic component of the electron pressure tensor, whereas smaller and more slowly at the collisional side induced by only the resistivity.

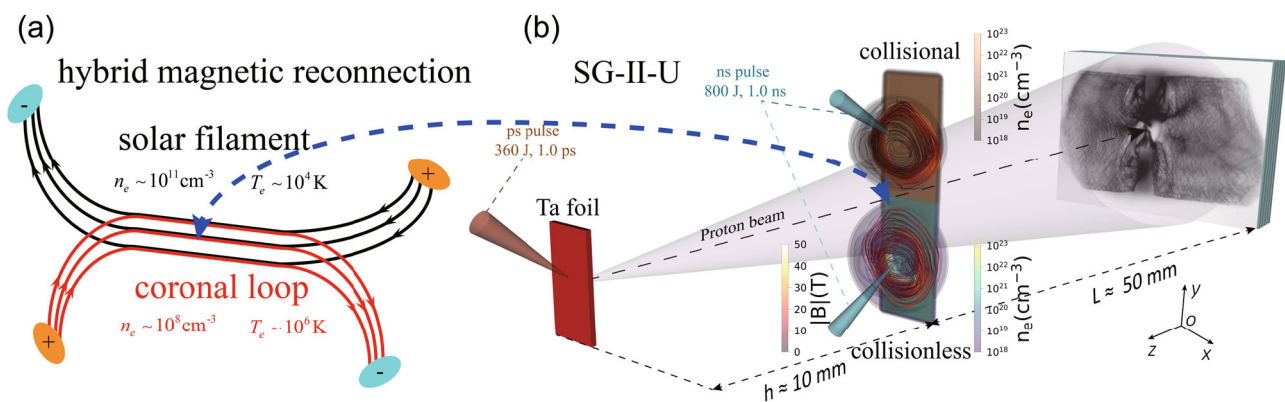


Fig. 1 Hybrid collisional-collisionless magnetic reconnection configurations and experimental set-up. **a** Magnetic reconnection in the hybrid regime between the collisional solar filaments and the nearby collisionless coronal loops. **b** Setup for the experiment on magnetic reconnection in the hybrid collisional-collisionless regime, which is achieved by irradiation of Cu (yellow) and CH (C_2H_2 , green) foil targets respectively with long ns laser pulses synchronously. Proton radiography is set up along the face-on ($-z$ -axis) direction for probing the magnetic field topology changes during the reconnection process, where the high-quality proton beam is generated from a tantalum foil target driven by the relativistic ps laser pulse, see Methods.

Results

Experimental setup. The hybrid magnetic reconnection experiments are carried out on the ShenGuang II Upgrade (SG-II-U) laser facility that has 8 ns pulses and 1 relativistic ps pulse. Figure 1b shows a diagram of the experimental setup, where the asymmetric collisional-collisionless reconnection is achieved by irradiation of Cu and CH foil targets respectively with long ns laser pulses synchronously. The ablated low-Z CH plasma is in the collisionless state, while the high-Z Cu plasma is in the collisional state, due to their different ionization charge states. These two plasmas expand and collide with each other, forming the magnetic reconnection in the hybrid regime, because both of them advect the self-generated Biermann magnetic fields together, as also shown in 1b (see the density maps and field lines). In order to balance the aspect ratio of the current sheet L/δ and the relative velocity of the plasma bubbles, the distance between the two focal spots is appropriately set to be 1.8 mm. The temporally and spatially highly-resolved proton radiography is set up along the face-on ($-z$ -axis) direction for probing the magnetic field topology changes during the reconnection process, where the high-quality proton beam is generated by target normal sheath acceleration from a tantalum foil target driven by the relativistic ps laser pulse. For improving the quality of the proton beam, we optimized the thickness of the backlight target to $20 \mu\text{m}$, meanwhile, for reducing the scattering of protons, a 0.5 mm gap was left between the Cu and CH targets, and the commonly used mesh-grid has been removed to reduce blurring. The static radiography images clearly show that the proton beam is of high quality with almost uniform distributions, where the cut-off energy exceeds 30 MeV , see Supplementary Note 1 and Fig. 1. For protons with energy of typically 13.5 MeV , we estimate the time for them to pass through the reconnection region is about 20 ps , far less than the characteristic plasma evolution time (generally $\sim \text{ns}$), so that the transient radiography can be guaranteed.

Features of self-generated Biermann magnetic fields. To have an intuitive understanding of the self-generated Biermann magnetic fields in laser-driven expanding plasmas, we firstly take proton radiography for a single CH plasma bubble. The radiography images are shown in Fig. 2a, b at time $t = 0.7$ and 1.0 ns , respectively, which correspond to the radiography protons of 13.5 and 7.7 MeV . We see that the protons are deflected into the inside of the plasma bubble and a clear low-dose ring structure is formed on the periphery of the plasma bubble, which can be regarded as the direct evidence for generation of a toroidal, clockwise Biermann magnetic field. Note that, if it is a radial electric field, the protons should be deflected outside the plasma bubble³². Further, comparing 2a, b, we can also estimate the plasma expansion velocity parallel to the target surface is about $700 \text{ km} \cdot \text{s}^{-1}$ ³³, as about $2.0 c_s$, where $c_s \equiv (\gamma \bar{Z} T_e / m_i)^{1/2}$ is the ion sound speed. Similar radiography images of laser-ablated Cu plasmas are also obtained, by which we estimate that its expansion velocity is on the same order due to the similar charge-to-mass ratio \bar{Z}/A . These self-generated Biermann magnetic field topologies are also verified by our three-dimensional (3D) synchronous proton radiography experiment (unpublished).

To extract more quantitative information from the radiographs, we use the inverse field-reconstruction code “PROBLEM”³⁴ to recover the path-integrated magnetic fields ψ , see Methods. Reconstructed ψ for the dashed-box region in Fig. 2a and b are shown in 2c and d respectively, which further confirms the existences of toroidal magnetic fields in expanding plasmas (see red dashed curves). The value of ψ is about $4.0 \text{ T} \cdot \text{mm}$, from which we can estimate the average field strength about $> 10 \text{ T}$. This is in good consistence with the estimation

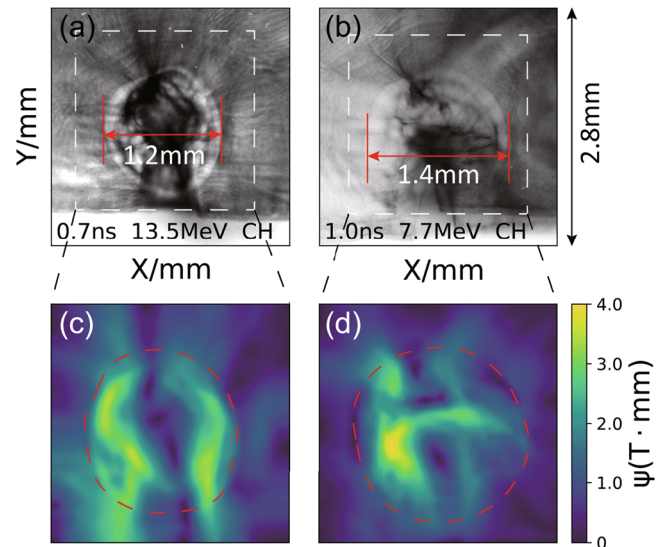


Fig. 2 Topologies of self-generated Biermann magnetic fields in laser-driven expanding CH plasma bubbles. **a** and **b** are respectively the face-on proton radiography images at $t = 0.7 \text{ ns}$ and 1.0 ns for CH plasma expansion, where the higher the grayscale represents the higher the proton doses. **c** and **d** are the strength of the reconstructed path-integrated magnetic fields ψ (in units of $\text{T} \cdot \text{mm}$), corresponding to the dashed-box region in **(a)** and **(b)** respectively.

under paraxial approximation, where the path-integrated magnetic field ψ is estimated^{15,21,22} as

$$\psi(\text{T} \cdot \text{mm}) \equiv \int_0^d \mathbf{B} dz \approx 0.1445 \frac{w(\mu\text{m}) \sqrt{E_p(\text{MeV})}}{L(\text{mm})}, \quad (1)$$

where w and L are respectively the width of the low-dose ring and the distance from the plasma to the RCF stack, and E_p is the proton energy. Assuming $w \sim 500 \mu\text{m}$, $E_p \sim 13.5 \text{ MeV}$ and $L \sim 50 \text{ mm}$ for CH plasma in 2a, the magnetic field is roughly estimated as $\psi \approx 5.3 \text{ T} \cdot \text{mm}$, and the field in 2b at $t = 1.0 \text{ ns}$ is about $7.6 \text{ T} \cdot \text{mm}$.

Hybrid collisional-collisionless magnetic reconnection: experimental results. The proton radiography results of the magnetic field topologies at various times in Fig. 3a–d provide direct picture of the whole process for the magnetic reconnection in this asymmetric regime. At time $t = 0.3 \text{ ns}$ (Fig. 3a), we see that the toroidal Biermann magnetic field still has not sufficiently developed and is not prominent, where some small-scale jet-like proton accumulations exist possibly due to the filamentary magnetic field arising from escaping of hot electrons³⁵. At time 1.0 ns (Fig. 3b), two low-dose rings (marked by the blue dashed lines) form at respectively collisionless CH and collisional Cu plasmas, which indicate the toroidal Biermann magnetic fields form, similar to those in Fig. 2a, b. We also see that the two magnetic fields already start to touch each other, consistent with the above estimations of their expansion velocities. Further, we see that more protons accumulate inside the Cu plasma bubbles than that of CH, indicating a stronger self-generated magnetic field, which is attributed to a steeper temperature gradient ∇T_e of Cu plasmas, see Supplementary Note 2 and Fig. 2. Also, the sharper proton accumulation radiography in CH plasmas may benefit from the uniform drive laser focal spot in our experiment, rather than the Gaussian one in Cu plasmas.

At later time $t = 1.5 \text{ ns}$ [3(c)], both Cu and CH plasmas continue to flow in, and as a result, the anti-parallel magnetic

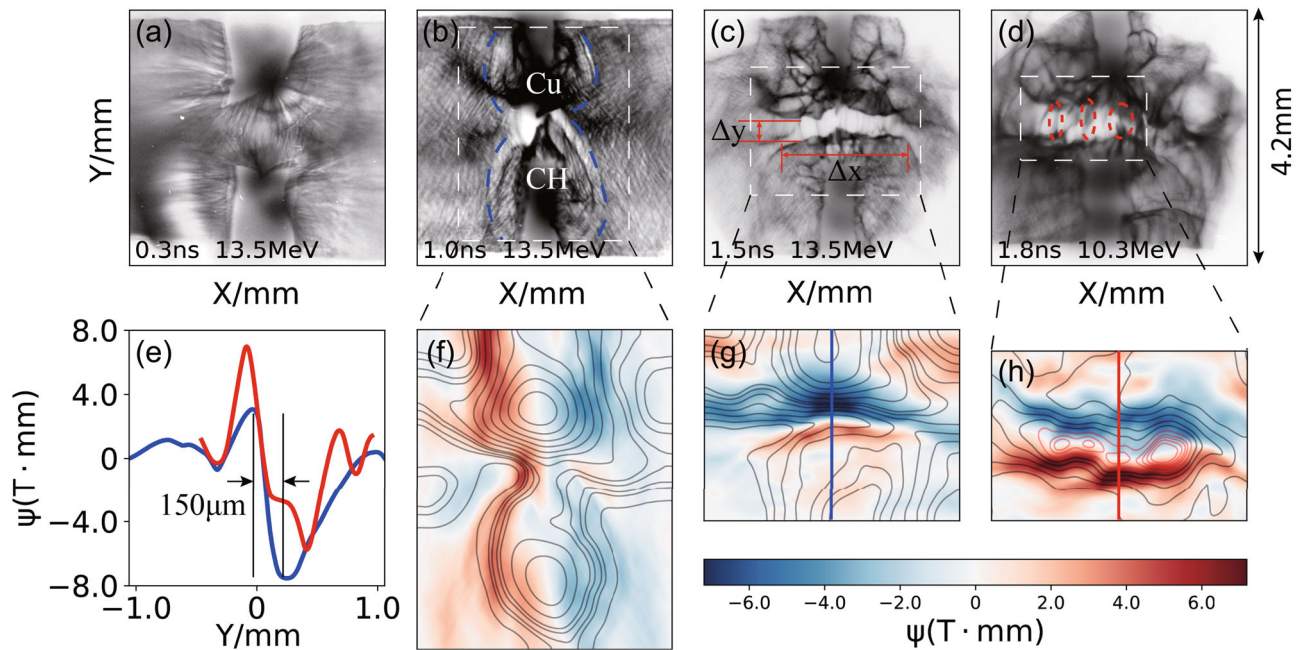


Fig. 3 Experimental results of hybrid collisional-collisionless magnetic reconnection. **a–d** are the proton radiography results of magnetic field topologies at time $t = 0.3, 1.0, 1.5$ and 1.8 ns respectively, where the upper half is for collisional Cu plasma and the lower is for collisionless CH. The higher the grayscale represents the higher the proton doses, and all images are rescaled to the realistic length through dividing by the radiography geometric magnification $M = 6.0$, see Methods. **f–h** are the reconstructed path-integrated magnetic fields ψ , corresponding to the dashed-box region in **(b–d)** respectively, where the color map in **(f)** represents B_y component and those in **(g)** and **(h)** represent B_x components. The contour lines in **(f–h)** represent the corresponding vector potential A_z . **(e)** shows the profiles of ψ in **(g)** (blue line) and **(h)** (red line) along y -axis.

fields are strongly squeezed in their colliding region forming a reconnection current layer. Correspondingly, the proton radiography image (Fig. 3c) shows that two low-dose rings merge into a long and narrow ribbon with length $\Delta x_{\text{exp}} \sim 1.9$ mm and width $\Delta y_{\text{exp}} \sim 0.3$ mm. Almost all protons are deflected out of this narrow ribbon region indicating that rather strong magnetic field exist locally, and the Y-shaped opening ends at both side of the ribbon region imply that the magnetic fields in Cu and CH plasmas begin to separate³⁶. Finally and more importantly at time $t = 1.8$ ns [3(d)], we see that the uniform low-dose ribbon is disturbed, and several high-dose fine filaments appear (marked by the red-dashed circles), which means that protons pass through without significant deflection. In other words, it means that the magnetic fields are dissipated at these fine filamentary regions, which is the key evidence for the occurrence of magnetic reconnection.

To more accurately reflect the change of the magnetic field topology, the reconstructed path-integrated magnetic field ψ and the corresponding vector potential A_z (see field lines) are shown in Fig. 3f–h, see Methods. They clearly show that the two toroidal magnetic fields [see 3f] are piled up together, forming a narrow reconnection layer dominated by only the anti-parallel B_x component [see Fig. 3g], the field strength at the center tends to zero. As shown in Fig. 3e for the profile of ψ along y -axis, we see that the asymmetry of the plasma properties results in the asymmetric magnetic flux (blue curve), which is stronger in Cu ($y > 0$) than CH ($y < 0$). And at later time, the current sheet on the side of the Cu plasma is obviously widened than that in CH plasmas (red curve), which may be the result of the magnetic diffusion caused by the strong collision effect. Using the Ampere’s law $\mathbf{J} = \nabla \times \mathbf{B}/\mu_0$, it is estimated that the width of the current sheet (peak to peak) is about $2\delta_{\text{exp}} \sim 150 \mu\text{m}$, which is much smaller than the length $2L \sim 1.9$ mm. For such a long and narrow current sheet, the tearing instability occurs and develops rapidly,

resulting in formation of multiple plasmoids^{27–29}, which are shown clearly in 3(h) by the red contours, also corresponding to the high-dose filaments in the radiography image 3d. Further, we see that there are still lots of un-reconnected magnetic fluxes on the outside of the fragmented current sheet, which may be due to the inefficient plasmoid ejection (because of high β) prevents further inflow of upstream magnetic fields^{30,31}. Compared with other published CH-CH reconnections^{15,17,22}, due to the optimized proton radiography, we observed a clear current sheet and plasmoid structure. Meanwhile, compared with reconnections with stronger collisionality (such as Al-Al and Au-Au)¹⁴, the current sheet in our experiment is more unstable to the tearing instability. In view of the above radiography results, we conclude that we have directly observed the growth of the tearing instability and formation of multiple plasmoids as well as the whole reconnection dynamics in the plasmoid-dominated magnetic reconnection.

Hybrid collisional-collisionless magnetic reconnection: simulation results. The above experimental results are reproduced and explained by a self-consistent combination of RMHD and PIC simulations as well as the proton radiography iterative inversion algorithm. As mentioned, magnetic reconnection is a rapid process of global magnetic topological self-organization triggered by local reconnection points, which depends critically on the plasma states. Before two plasma interactions, the laser-ablated plasma expansion dynamics is majorly governed by RMHD. Therefore, we firstly run the RMHD simulations with the “FLASH” code³⁷ to obtain the basic plasma parameters as the initial condition for the following PIC simulations that can describe the interaction and reconnection dynamics of two plasmas. The expanding Cu and CH plasma parameters obtained from RMHD simulations are summarized in Table 1a, where the electron density n_e , temperature T_e , flow velocity v and magnetic field strength B are all taken for those at the periphery of each plasma bubble. The

Table 1 Plasma parameters obtained from radiation-magnetohydrodynamic (RMHD) and following self-consistent particle-in-cell (PIC) simulations.

(a) plasma parameters obtained from 3D RMHD simulations		(b) plasma parameters in the reconnection layer obtained from PIC simulations	
para	T_e (keV)	Z	v (km·s ⁻¹)
Cu	1.5 ± 0.2	20 ± 2	800 ± 100
CH	1.1 ± 0.1	3.5	1000 ± 100
	n_e (10 ¹⁸ cm ⁻³)	B (T)	β
	2.5 ± 1.0	40 ± 10	1.0 ± 0.2
	8.0 ± 3.0	25 ± 10	5.7 ± 1.0
	T_i (keV)	v_A (km·s ⁻¹)	β_{ram}
	2.5 ± 0.5	200 ± 50	6.7 ± 1.0
	2.5 ± 0.5	130 ± 30	50 ± 10
	n_e (10 ¹⁸ cm ⁻³)	B (T)	S
	30 ± 15	100 ± 20	1500 ± 500
	40 ± 20	50 ± 10	5000 ± 1500
	T_e (keV)	λ_{ei} (μm)	d (μm)
	2.5 ± 0.5	100 ± 40	60 ± 10
	2.5 ± 0.5	500 ± 200	25 ± 10
	δ_{sp} (μm)	δ_{sp} (μm)	ρ_e (μm)
	15 ± 5	15 ± 5	70 ± 20
	R_m	R_m	R_m
	8000 ± 2000	8000 ± 2000	3000 ± 500
	120 ± 30	120 ± 30	12000 ± 3000
	β	β	P_e
	1.0 ± 0.2	4.0 ± 2.0	0.03 ± 0.02
	5.7 ± 1.0	16 ± 5.0	0.05 ± 0.03

(a) The expanding Cu and CH plasma parameters at $t = 0.8$ ns obtained from the three-dimensional (3D) RMHD simulations, which are used as the initial condition for the following PIC simulations after self-similar scaling. (b) The plasma parameters inside the compressed reconnection layer (current sheet) of respectively Cu and CH sides at $t = 1.3$ ns obtained from PIC simulations, which are exactly the plasma states for magnetic reconnection. The listed plasma parameters include electron density n_e , electron temperature T_e , ion charge state Z , magnetic field B , plasma flow velocity v and Alfvén speed v_A , the ratio of thermal pressure to magnetic pressure β , the ratio of ram pressure to magnetic pressure β_{ram} , Reynolds number R_m , magnetic Reynolds number R_m and Peclet number P_e , electron mean free path λ_{ei} , Lundquist number S , current sheet width of the Sweet-Parker model δ_{sp} , ion skin depth d_i and ion cyclotron radius ρ_e . When calculating R_m , R_m , and P_e , the plasma scale and Coulomb logarithm are taken as 1.0 mm and 10.0, respectively, and the half length of the current sheet is estimated to be $L = 10$ mm when calculating S and δ_{sp} .

expansion velocities and magnetic fields are comparable to the experimental results shown in the Fig. 2 above, and the electron density and temperature are also close to those measured by optical interferometry³⁰ and Thomson scattering¹⁴. More details can also be seen from the Methods and Supplementary Fig. 2. The differences in the equation of state (EOS)³⁸ and opacity³⁹ of the Cu and CH lead to the asymmetric plasma states on both sides. For both plasmas, the thermal pressure to magnetic pressure ratio $\beta > 1$ and the ram pressure to magnetic pressure ratio $\beta_{ram} \gg 1$ indicate that reconnection is strongly driven^{21,22}.

For the following plasma colliding and reconnection process, due to low densities and high temperatures of plasmas at their interaction region, the electron mean free path λ_{ei} comparable to the plasma scale L , therefore, the kinetic effects start to play key roles and kinetic PIC simulations are required^{40–42}. In order to connect the PIC simulation with the RMHD simulation in a self-consistent manner, a self-similar transformation is proposed and applied here, see more details in Methods. Just like the self-similarity principle of the magnetohydrodynamic equations^{43–45}, we choose a set of free parameters to spatially scale down the plasma parameters obtained from the above RMHD simulation to the relative small scale that is practical for kinetic PIC simulation, where the plasma properties including β , β_{ram} , the Mach number and the Alfvén Mach number, etc., are all kept conserved between RMHD and PIC. In order to correctly evaluate the relative strength of Coulomb collisions⁴⁶, we ensure that L/λ_{ei} remains unchanged in the two systems. Through this methodology, we carry out the whole simulation in a self-consistent manner.

After the Cu and CH plasmas collide, the supersonic inflow makes the plasma and magnetic fields pile up around the reconnection region, and the properties of the plasmas (electron density n_e , temperature T_e) and fields become almost uniform in the z -direction, see Supplementary Fig. 3. These make the magnetic reconnection quasi-2D, and this reconnection process can be approximated with kinetic 2D3V PIC simulations. In addition, it has also been identified that the 3D tilted geometric effect has little effect on the reconnection rate in such a strongly-driven regime²².

The fully-kinetic PIC simulations are performed in two-dimensional (2D) xy plane with the code “EPOCH”⁴⁷. Topologies of magnetic field evolutions at various times in the simulations are shown in Fig. 4a–d from $t = 1.0$ to 1.8 ns (following the previous RMHD simulation). Based on these field topologies, we also carry out the simulation for the synthetic proton radiography process, see Methods. The synthetic proton radiography images corresponding to 4a–d are shown respectively in Fig. 4e–h. We see that the Cu and CH plasma bubbles start to contact with each other at $t = 1.0$ ns [Fig. 4a], in consistence with the experimental result [see Fig. 3b]. The corresponding synthetic radiography image in Fig. 4e also show similar feature as that in the above 3b, where the slight difference may be due to lack of a driving source. At $t = 1.2$ ns [Fig. 4b], similar as the experimental results, we see that the magnetic fields are compressed and amplified in the colliding region, forming a long and narrow current sheet. Due to the plasma pressure asymmetry, we also see the current sheet drifts slowly towards the Cu plasma side.

Subsequently at time $t = 1.5$ ns, we see clearly from Fig. 4(c) that the current sheet breaks and multiple plasmoids form due to the tearing instability^{27–29}, and magnetic field energy dissipates at several local points (X-points), marked by the red crosses. Furthermore, we see all the plasmoids protrude into the CH plasma side and are more pronounced in the CH plasma side, which further verifying that the asymmetry of the tearing instability and magnetic reconnection. This feature is quite similar to the astronomical observations of the reconnection

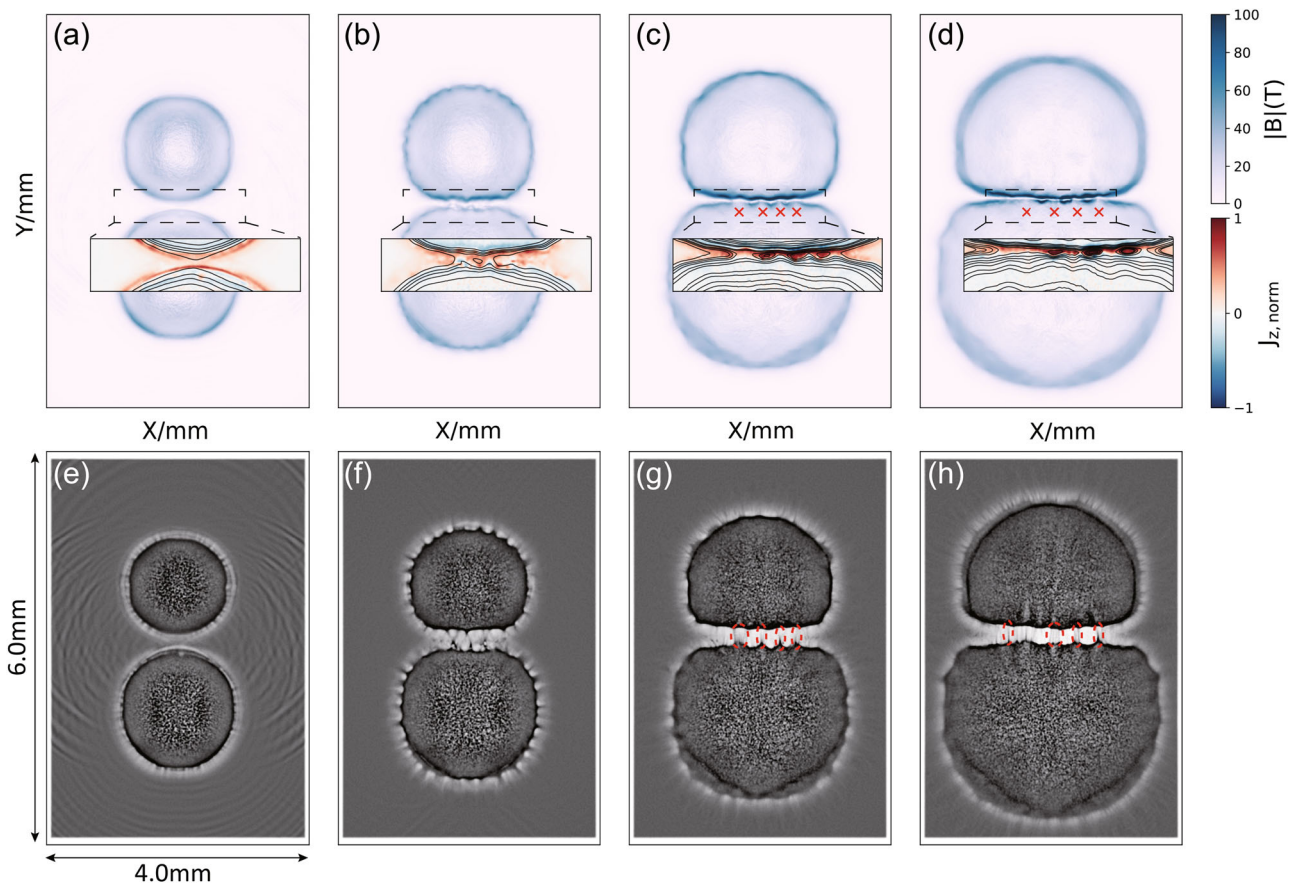


Fig. 4 Kinetic 2D3V particle-in-cell (PIC) simulation results of the hybrid magnetic reconnection. Here the initial conditions are taken from the RMHD (radiation-magnetohydrodynamic) simulation at $z = 400 \mu\text{m}$, and at $t = 0.8 \text{ ns}$ [See Supplementary Fig. 2]. **a–d** are distributions of the magnetic field strengths $|B|$ (in white-blue color bar) at time $t = 1.0, 1.2, 1.5, 1.8 \text{ ns}$ respectively during the magnetic reconnection. The zoomed images show the out of plane current densities J_z (in blue-red color bar, normalized to $1 \times 10^{14}, 4 \times 10^{14}, 6 \times 10^{14}, 10 \times 10^{14} \text{ A} \cdot \text{m}^{-2}$ respectively) and vector potential A_z (contours) of the reconnection region, corresponding to the dashed box regions in **(a–d)** respectively. **e–h** show the corresponding synthetic proton radiography images based on the magnetic fields **(a–d)** obtained from PIC simulations (more details see Methods), where the higher the grayscale represents the higher the proton doses. The radiography geometric magnification M and proton energy E_p are consistent with the realistic experimental radiography setup. In order to match the extracted path-integrated magnetic fields ψ , the thickness of the fields is taken as $d \sim 100 \mu\text{m}$.

between solar filaments and coronal loops¹³. Again, both the X-points and plasmoids can be accurately reflected by the synthetic proton radiography, as shown in Fig. 4g, where several high-dose fine filaments appear (marked by the red-dashed circles), agreeing well with the experimental results in Fig. 3c, d, although the spatial averaging effect reduces the clarity of the experimental images. Note that the length and width of the low-dose ribbon in 4g is about $\Delta x_{\text{sim}} \sim 1.7 \text{ mm}$ and $\Delta y_{\text{sim}} \sim 0.25 \text{ mm}$, which are also both consistent with the experimental results. At much later time $t = 1.8 \text{ ns}$ [Fig. 4d], we see that the magnetic fields, current sheet and plasmoids are further continuously compressed, and the distance between these plasmoids gradually increases due to stretch and ejection^{30,31} ($v \sim 10^5 \text{ m} \cdot \text{s}^{-1}$). These plasmoids and X-points (high-dose filaments) become more prominent in radiographic images, see Figs. 4h and also 3d. The number of plasmoids and X-points does not change with time, implying that the merging of magnetic islands and secondary tearing instability^{25–29} both do not occur here. The phenomenological consistency between the simulation and the experimental results verifies that the tearing instability and plasmoid-dominated magnetic reconnection indeed take place in our experiment.

To reveal the inherent mechanism of the hybrid collisional-collisionless magnetic reconnection, the main parameters of both

Cu and CH plasmas inside the reconnection layer obtained from PIC simulations are summarized in Table 1b, which are exactly the plasma states for magnetic reconnection. We see that since both Cu and CH plasmas are highly compressed, their densities and temperatures significantly increase, and the magnetic field strengths are amplified to more than 2 times than their initial values, see also Supplementary Note 3 and Fig. 4. The average width of the reconnection layer (current sheet) is about $2\delta_{\text{sim}} \sim 100 \mu\text{m}$, which is similar with the reconstructed experimental result $2\delta_{\text{exp}} \sim 150 \mu\text{m}$. The Lundquist number $S \equiv Lv_A/\eta \gg 1$ in both plasmas, especially in the CH plasma where $S \sim 0.5 \times 10^4$, verifying that the tearing instability can easily occur and develop. But they are still well below the threshold ($S \sim 10^7$) at which the current sheet thinning becomes significant^{48,49}, i.e. the current sheet remains in the relatively static Sweet-Parker regime. The half width of the Sweet-Parker current sheet $\delta_{\text{sp}} \equiv L/\sqrt{S}$ of Cu (about $0.4d_i$) and CH (about $0.3d_i$) plasmas are both smaller than the ion skin depth d_i or ion cyclotron radius ρ_{ci} , which means the two-fluid effect^{22,36} needs to be considered. More importantly, we see that, due to the very different ion charge states \bar{Z} of Cu ($\bar{Z} \approx 20$) and CH ($\bar{Z} \approx 3.5$), the plasma on the Cu side is in a strongly-collisional state ($\lambda_{ei} \sim 100 \mu\text{m}$ and $\lambda_{ei}/2\delta_{\text{exp}} \sim 0.67$), while the plasma on the CH side is collisionless ($\lambda_{ei} \sim 500 \mu\text{m}$ and $\lambda_{ei}/2\delta_{\text{exp}} \sim 3.33$). Comparing δ_{sp} and λ_{ei} in Cu

and CH plasmas, and take into account the experimental current sheet width $2\delta_{\text{exp}} \sim 150 \mu\text{m}$, it can be considered that the asymmetry of reconnection is mainly reflected in Coulomb collisions. That is, an asymmetric magnetic reconnection in the hybrid collisional-collisionless regime can be expected.

From both the above experimental and simulation results [comparing Fig. 3c, d, or comparing 4c and d], we estimate that the characteristic growth time of the tearing instability for the hybrid reconnection is rather fast as about $\tau_{\text{TI}} \sim 0.5 \text{ ns}$, at the same order of the Alfvén transit time across the current sheet $\tau_A \equiv \delta/v_A$. Such fast tearing instability and reconnection dynamics cannot be explained by only the two-fluid effect. This can be proved from two aspects. One the one hand, as known, the maximum growth rate of the spontaneous tearing instability from the hydrodynamic perspective is about $\gamma_{\text{max}} \sim (v_A/\delta)(d_e/d_i)^{0.7}(d_i/\delta)^{1.5}$ ^{50,51}. Substituting the reconnection plasma parameter in Table 1b into it and assuming $\delta \sim 50 \mu\text{m}$, we estimate that $\gamma_{\text{Cu}} \sim (2.5 \pm 1.0) \times 10^8 \text{ s}^{-1}$ and $\gamma_{\text{CH}} \sim (1.5 \pm 0.5) \times 10^8 \text{ s}^{-1}$, which corresponds to the characteristic growth time of the tearing instability as both larger than 10 ns, too slow to explain the experimental and simulation results. On the other hand, considering only the two-fluid effect, the predicted most unstable mode is $k_{\text{max}} \sim (1/\delta)(d_e/d_i)^{0.3}(d_i/\delta)^{0.5}$ ^{50,51}, which means that the most confident number of X-points in reconnection is $M = Lk_{\text{max}}/\pi \sim 2$, also smaller than 4 observed in our experiment (see Fig. 3c).

Therefore, to explain the fast and effective tearing instability observed in our experiment, we analyze the various contributions of the dissipative reconnection electric field E_z , which after normalization is defined as the reconnection rate. The two main contributions, the non-gyrotropic component of the electron pressure tensor $E_{z,p_e} \sim -\nabla_y P_{yz}/(en_e)$ and the resistive component $E_{z,\eta} = \eta J_z$ are shown in Fig. 5a, b respectively at time $t = 1.4 \text{ ns}$. Their contributions varying with time from $t = 1.2$ to 1.6 ns for respectively Cu and CH plasmas during reconnection are also shown in Fig. 5c. We see clearly that the non-gyrotropic electron pressure tensor always dominates [the lower half part in Fig. 5a and the blue square symbol in Fig. 5c] in the collisionless CH plasma side, while the resistive electric field dominates [the upper half part in Fig. 5b and the red triangle symbol in Fig. 5c] in the

collisional Cu plasma side. And as a whole, for the hybrid reconnection, the collisionless nongyrotropic electron pressure tensor contributes (about 75%) most of the reconnection electric field, while the resistivity only contributes $\sim 25\%$. In other words, it is just the collisionless non-gyrotropic electron pressure that results in the fast tearing instability and reconnection in our experiment⁵². The total reconnection electric field is about $E_z \sim 6 \times 10^6 \text{ V} \cdot \text{m}^{-1}$, on the order of $0.3 \pm 0.1 v_{A,\text{loc}} B_{\text{loc}}$ after normalization [marked by the green circle in Fig. 5c], i.e., a fast reconnection rate^{40,42}.

To further demonstrate the dynamics of the hybrid reconnection, we also carry out RMHD-PIC simulations for the cases of the purely collisionless CH-CH and purely collisional Cu-Cu magnetic reconnection, where the drive laser and other parameters are also the same. The results are shown in Supplementary Note 4 and Fig. 5. We see that in the purely collisionless reconnection case, the tearing instability grows even more quickly, resulting in the formation of more number of multiple X-points, where the normalized reconnection electric field is $E_z \sim 0.5 \pm 0.05 v_{A,\text{loc}} B_{\text{loc}}$ [marked by the green star in Fig. 5c], a little higher than the hybrid case. By contrast, in the purely collisional Cu-Cu reconnection case, the resistive electric field dominates, a Sweet-Parker-like current sheet with single X-point is formed, where $E_z \sim 0.16 \pm 0.03 v_{A,\text{loc}} B_{\text{loc}}$ [marked by the green diamond in Fig. 5c] is much lower. These further confirm the possibility of the occurrence of a hybrid collisional-collisionless magnetic reconnection in our experiment.

Conclusions

In summary, we have carried out the well-designed experiment on an unexplored new regime of magnetic reconnection, hybrid collisional-collisionless regime, by colliding of laser-ablated high-Z Cu and low-Z CH plasmas. Using highly-resolved proton radiography, we have directly observed the topology changes for the whole process of the plasmoid-dominated magnetic reconnection. With the self-consistent RMHD-PIC simulations, we find that the experimental reconnection indeed lies in the hybrid regime and the growth rate of the tearing instability is still extremely large, resulting in rapid formation of multiple

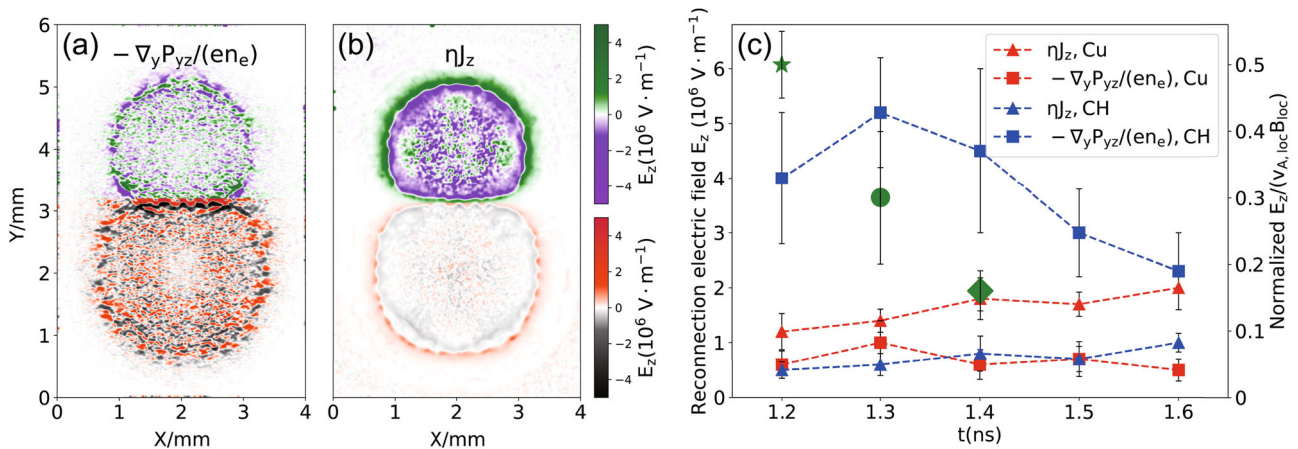


Fig. 5 Contribution terms of the reconnection electric field E_z in the hybrid magnetic reconnection. **a** and **b** are respectively the contributions from the off-diagonal (nongyrotropic) component of the electron pressure tensor $E_{z,p_e} \sim -\nabla_y P_{yz}/(en_e)$ and the resistivity $E_{z,\eta} = \eta J_z$ at $t = 1.4 \text{ ns}$, where, the same as the setup in experiment, the upper half part is collisional Cu plasma (where E_z is quantified using the colormap scale from purple to green colors) and the lower half part is collisionless CH plasma (where E_z is quantified using the colormap scale from black to red colors). **c** shows their contributions varying with time from $t = 1.2$ to 1.6 ns for respectively Cu and CH plasmas during reconnection, the error bars represent one standard deviation. The normalized reconnection electric field E_z (normalized to local Alfvén speed $v_{A,\text{loc}}$ and magnetic field B_{loc}) for respectively the cases of purely collisionless CH-CH (green star), hybrid Cu-CH (green circle) and purely collisional Cu-Cu (green diamond) reconnections are also marked in **(c)**, where all the values are chosen at the time when the changes of their magnetic field topologies are most significant.

plasmoids, lower than the purely collisionless case but much higher than the collisional case. We show that, in this asymmetric magnetic reconnection, the reconnection electric field shows much distinct feature, which is large and grows fast at the collisionless plasma side induced by the off-diagonal (non-gyrotropic) component of the electron pressure tensor, whereas smaller and more slowly at the collisional side induced by only the resistivity.

The hybrid collisional-collisionless magnetic reconnection discussed here occurs widely in astrophysics. For example, for the reconnection between the erupting collisional filaments and the collisionless coronal loops in solar and stellar atmosphere, the astronomical observations reveal that most of the plasmoid formation and plasma heating occurred on the side of the collisionless coronal loops¹³, are qualitatively consistent with our results. Besides, the possible reconnections occurring between the dense accretion disk and the tenuous interstellar medium may also be in such hybrid regime. Our experimental results show that the plasmoid formation is a universal feature of magnetic reconnection, even in this hybrid regime, which has been recently observed to help facilitate the slow-to-fast phase transition of reconnection in the solar atmosphere⁵³. We also show that the specific magnetic reconnection mechanism depends critically on the plasma collision rates, which significantly affect the growth of the tearing instability and further the global reconnection rate, eventually determining the energy conversion efficiency from fields to plasmas, such as heating the solar corona³. Moreover, the lower plasma β , higher Lundquist number S and ubiquitous guiding fields in these astrophysical environments may promote the plasmoid ejection, thereby help to establish the positive feedback for global fast reconnection^{25,26}.

However, under this experimental scheme, our experimental results are still relatively preliminary. Although we have demonstrated general features of this hybrid reconnection regime, such as current sheets and plasmoids, using proton photography, a direct and detailed comparison with purely collisional and collisionless reconnection remains for future work. There have been a large number of plasma parameter measurements, but, how to quantitatively characterize the collisionality experimentally remains a problem. Furthermore, how to create plasmas and magnetic reconnection with greater differences in collisionality is also a technical challenge. In view of this, our proposal and research can be seen as the first attempt to answer these questions experimentally, and will attract more attention to this hybrid reconnection regime.

Methods

Experimental setup. The hybrid collisional-collisionless magnetic reconnection experiments presented in this work are carried out on ShenGuang II upgrade (SG-II-U) laser facility at the Joint Laboratory on High Power Laser and Physics, Shanghai Institute of Optics and Fine Mechanics, Chinese Academy of Sciences. The laser facility has 8 nanosecond (ns) pulses and 1 picosecond (ps) petawatt pulse. The main target consists of two foils with the upper half part as Cu foil of density $\rho = 8.92 \text{ g} \cdot \text{cm}^{-3}$ and the lower half part as plastic CH foil of density $\rho = 1.02 \text{ g} \cdot \text{cm}^{-3}$. Both foil targets have thickness of $30 \mu\text{m}$ and width of 1.0 mm , and parallel to each other, and there is a 0.5 mm gap between the Cu and CH targets, in order to eliminate the scattering effect of protons by the solid targets.

The two foil targets are ablated with two 3ω long laser pulses (green) that have energy about $800 \pm 100 \text{ J}$ in a $1 \pm 0.1 \text{ ns}$ square temporal profile, with either a $200 \mu\text{m}$ FWHM Gaussian or a $450 \mu\text{m}$ diameter uniform focal spot. The corresponding average laser intensities are about $2.5 \times 10^{15} \text{ W} \cdot \text{cm}^{-2}$ and $4.0 \times 10^{14} \text{ W} \cdot \text{cm}^{-2}$ respectively. The incident angle between the laser beam and the target normal is about 45° , and the distance between the two focal spots is about 1.8 mm . The proton radiography is set up along the face-on ($-z$ -axis) direction, by irradiating the backlighter $20\text{-}\mu\text{m}$ -thick Ta foil (red) target with a relativistic ps pulse. The ps pulse has energy of $350 \pm 50 \text{ J}$, wavelength of $1.053 \mu\text{m}$, duration of $1.0 \pm 0.1 \text{ ps}$ and is focused by a 800 mm focal-length, $f/2.5$ off-axis parabolic mirror to an intensity about $3.0 \times 10^{19} \text{ W} \cdot \text{cm}^{-2}$, with focal spot diameter $\sim 40 \mu\text{m}$. The cut-off energy of the high-quality laminar proton beam exceeds 30 MeV , and the deflected protons are finally deposited on the HD-V2 radiochromic film (RCF) stack, whose response

to proton dose has been well calibrated with a good linear relationship between proton dose and optical density (OD). The distance between the backlighter foil (Ta) and the main foils (Cu and CH) is $h \sim 10 \text{ mm}$, and that between the main foils and the RCF stack is $L \sim 50 \text{ mm}$, which result in the geometric magnification factor of the proton radiography system as about $M \equiv (h + L)/h \sim 6.0$.

Path-integrated field reconstruction. The extraction of the path-integrated magnetic field ψ from proton radiographs in this work is done by using the algorithm and program “PROBLEM”³⁴, where a parabolic Monge-Ampère equation is solved. Note that the formation of the proton radiographs can be understood as following.

First, the propagation of laser-produced proton beam initially can be regarded as a uniform expansion from a point source (laser-driven target normal sheath acceleration region) into the probing plasma region. Under the paraxial approximation, $l_p/r_i \ll 1$, when the proton beam arrives at the probing region, it can be regarded as a two-dimensional near-planar sheet, where l_p and r_i are respectively the plasma lateral length and the distance from the proton source to the plasma, in our experiments, $l_p \approx 1 \text{ mm}$ and $r_i = h \approx 10 \text{ mm}$.

Afterwards, the proton beam is deflected by the Lorentz force arising from self-generated magnetic fields in plasmas, and the lateral deflection velocity can be expressed as

$$\mathbf{v}(\mathbf{x}_{\perp 0}) \approx \frac{e}{m_p c} \hat{\mathbf{z}} \times \int_0^{l_p} ds \mathbf{B}(\mathbf{x}(s)), \quad (2)$$

where e is the proton charge, m_p is the proton mass, $\mathbf{x}_{\perp 0}$ and $\mathbf{x}(s)$ are respectively the initial perpendicular position and the proton trajectory. The outgoing proton beam moves approximately in a straight line at a constant velocity, and the lateral deflection velocity $\mathbf{v}(\mathbf{x}_{\perp 0})$ is amplified as

$$\mathbf{x}_{\perp}^{(s)}(\mathbf{x}_{\perp 0}) \approx \frac{r_i + r_s}{r_i} \mathbf{x}_{\perp 0} + \frac{\mathbf{v}(\mathbf{x}_{\perp 0})}{v_p} r_s, \quad (3)$$

where v_p is the proton velocity, r_s is the distance from the plasma to the RCF screen, $r_s = L \approx 50 \text{ mm}$ in experiments, and $\mathbf{x}_{\perp}^{(s)}$ is the proton position on the screen.

Eventually, the deflection effect by the magnetic field makes the initially uniform proton beam redistribute on the RCF screen as

$$\Psi(\mathbf{x}_{\perp}^{(s)}(\mathbf{x}_{\perp 0})) = \frac{1}{|\text{Det}(\nabla_{\perp 0}[\mathbf{x}_{\perp}^{(s)}(\mathbf{x}_{\perp 0})])|} \Psi_0, \quad (4)$$

where Ψ and Ψ_0 are respectively the redistributed proton flux on the RCF screen and the initial proton flux (generally uniform), and $\nabla_{\perp 0}$ is the gradient operator of the initial plasma coordinates.

Therefore, the path-integrated magnetic field can be obtained by solving the Monge-Ampère equation (4), and

$$\psi \equiv \int_0^{l_p} ds \mathbf{B}(\mathbf{x}(s)) = -\frac{m_p c}{e} \hat{\mathbf{z}} \times \mathbf{v}(\mathbf{x}_{\perp 0}). \quad (5)$$

Due to the divergence-free of magnetic field $\nabla \cdot \mathbf{B} = 0$, then the deflection velocity is curl-free $\nabla \times \mathbf{v} = 0$. The deflection velocity can be viewed as the gradient of a potential function $\mathbf{v} \equiv \nabla \phi$, and the corresponding magnetic field potential function is expressed as

$$\mathcal{A} = -\frac{m_p c}{e} \phi, \quad (6)$$

under the quasi-two-dimensional approximation, this is equivalent to the magnetic vector potential A_z , and $A_z \sim \mathcal{A}/l_z$.

This inversion problem is well-defined, the geometric distance and proton energy are determined in the experiments, the redistributed proton flux Ψ can be obtained from the response function of RCF optical density (OD) to proton dose, and which has an almost linear relationship in the low-dose region. The inhomogeneity of the initial proton flux Ψ_0 is ignored, see also Supplementary Fig. 1.

3D radiation-magnetohydrodynamic (RMHD) simulation. The three-dimensional (3D) RMHD simulations in this work are carried out by using the code “FLASH”³⁷, which has been developed to include many high energy density physics modeling capabilities including laser energy deposition, multi-temperature ($T_e \neq T_i \neq T_{\text{rad}}$), anisotropic electron thermal conductivity, and multi-group radiation transport etc. We have also further extended the code with the self-consistent magnetic field modeling capabilities including the Biermann battery, Nernst advection and so on, which is the reason why we called it as “RMHD”.

The initial conditions of 3D RMHD simulations are taken following those in the experiments. The size of the simulation box is $4 \times 6 \times 1.5 \text{ mm}^3$ in all (x, y, z) directions and the solid CH/Cu foil targets with thicknesses $30 \mu\text{m}$ in z direction and areas of $1.0 \times 2.0 \text{ mm}^2$ in respectively x and y directions are placed at the position $z = 0.2 \text{ mm}$. The ns laser pulses with energy of 800 J (a multiplier is used to account for the scattering caused by parameter instabilities and match the plasma morphology in the experiments), flat-top temporal profile of duration 0.9 ns plus

0.1 ns rising and falling times, and focal spots consistent with experiments are incident on the foil targets at an oblique angle of about 45°. The equation of state (EOS) and opacity of solid foil materials (CH and Cu) come from the code BADGER³⁸ and IONMIX³⁹, respectively. The initial densities of the solid foil targets are set to $\rho_{\text{CH}} = 1.02 \text{ g} \cdot \text{cm}^{-3}$ and $\rho_{\text{Cu}} = 8.92 \text{ g} \cdot \text{cm}^{-3}$, and the rest is filled with background He gas with a density of $2 \times 10^{-6} \text{ g} \cdot \text{cm}^{-3}$. All the initial temperatures are set to be uniform as room temperatures $T_0 \sim 290 \text{ K}$.

In the simulations, an adaptive grid is used. And the geometric-optical approximation of inverse bremsstrahlung absorption is used to represent laser heating. The Riemann solver of the MHD equations uses HLLC, and the slope limiter uses minmod. The Courant (CFL) number is self-adaptive, the typical value is 0.4. Fully implicit electron thermal conductivity is also adopted, and the flux limiter is selected as a typical 0.06. The boundary conditions for fluid, electron thermal conductivity and radiation transport are all set to open. The simulation results of plasma properties are shown in Supplementary Fig. 2.

Self-consistent RMHD-PIC simulation. The fully-kinetic PIC simulations in this work are performed in two-dimensional (2D) xy plane with the code “EPOCH”⁴⁷. It has been identified that the 3D geometric effect has little effect on the reconnection rate in such a strongly-driven regime²². In order to connect the PIC simulation with the RMHD simulation in a self-consistent manner, a self-similar transformation is proposed and applied. That is, before the kinetic effects become important, RMHD is used to simulate the macroscopic states of the plasmas, and then PIC is used to simulate the subsequent kinetic processes, while ensuring a self-consistent connection between them. Just like the self-similarity principle of the magnetohydrodynamic equations^{43–45}, we choose a set of free parameters to spatially scale down the plasma parameters obtained from the above RMHD simulation to the relative small scale that is practical for kinetic PIC simulation, where the plasma properties including β , β_{ram} , the Mach number and the Alfvénic Mach number, etc. are all kept conserved between RMHD and PIC. The Coulomb collisions are also well included by making L/λ_{ei} conserved.

The principle of this method comes from the self-similarity of the ideal MHD equations^{43–45}, that is, under a set of specific parameter transformation,

$$\begin{aligned} \mathbf{r}_1 &= a\mathbf{r}_0, & \rho_1 &= b\rho_0, & p_1 &= cp_0, \\ \mathbf{v}_1 &= \sqrt{c/b}\mathbf{v}_0, & \mathbf{B}_1 &= \sqrt{c}\mathbf{B}_0, & t_1 &= a\sqrt{b/c}t_0, \end{aligned} \quad (7)$$

the form of the ideal MHD equations remains unchanged. a , b and c are the free transformation parameters. \mathbf{r} , ρ , p , \mathbf{v} , \mathbf{B} and t respectively represent length, density, pressure, velocity, magnetic field and time. The subscripts 0 and 1 respectively represent two different systems connected by this parameter transformation. This means that under similar initial and boundary conditions, the two systems have the same evolution characteristics. This scale transformation is often used in laboratory astrophysics to compare experiment results with astrophysical events.

The condition for the establishment of this self-similarity is that the plasmas is polytropic and ideal, which means that viscosity, electric resistivity and heat conductivity are not dominant, i.e., the Reynolds number $Re \equiv Lv/\nu$, the magnetic Reynolds number $R_m \equiv Lv/\eta$ and the Peclet number $Pe \equiv Lv/\chi$ are far greater than 1.0. These dimensionless numbers, before the Cu and CH plasma bubbles touch each other, are listed in Table 1a. Both Re and R_m are far greater than 1.0. Although Pe is less than 1.0, considering that the plasma corona is approximately isothermal (see Supplementary Fig. 2) and the suppression of the electron heat flow by the magnetic fields, the coronal Pe will be greater than 1.0. And the coronal plasma is approximately an ideal gas, so it is also polytropic. Therefore, under limited approximations, the laser-driven expanding plasmas can be regarded as an ideal polytropic gas, where the self-similar transformation can be applied.

In the context of PIC simulations, since the plasma density has the relation $\rho \sim m_i n_i$ and pressure $p \sim nT$, the transformation parameters should be chosen as $b = f_m f_n$ and $c = f_n f_T$, where f_m , f_n and f_T are the transformation parameters of ion mass, plasma density and plasma temperature respectively. As for the transformation parameter a of length, in order to correctly account for the two-fluid effect, it should be ensured that L/d_i (on the order of 100 in typical laser-ablated plasmas) remains unchanged under the similar transformations, and this constraint gives $a = \sqrt{f_m/f_n}$, which also maintains compatibility with the Ampère’s law $\mathbf{J} = \nabla \times \mathbf{B}/\mu_0$. In this way, the self-similar transformation of ideal RMHD equations is self-consistently converted into the language of PIC simulation, that is, the transformation parameters a , b and c of RMHD variables are converted into f_m , f_n and f_T of PIC particle variables,

$$a = \sqrt{f_m/f_n}, \quad b = f_m f_n, \quad c = f_n f_T. \quad (8)$$

Other variables are also transformed according to the corresponding parameters, the fluid velocity $\mathbf{v}_1/\mathbf{v}_0 = \sqrt{f_T/f_m} = c_{s,1}/c_{s,0}$, i.e., the ratio of the ion sound velocity of the two systems. And the time $t_1/t_0 = f_m/\sqrt{f_n f_T} = f_m/\sqrt{c} = \omega_{ci,1}^{-1}/\omega_{ci,0}^{-1}$, the ratio of the ion cyclotron time of the two systems.

We apply this transformation methodology to the kinetic simulation of hybrid magnetic reconnection, and transform the results of the RMHD simulation at $t = 0.8 \text{ ns}$ to the PIC simulation, see Supplementary Fig. 2 and Supplementary Fig. 4. Balance the computing power and the universality, we choose the mass of Cu ions in the PIC simulation to be $m_{\text{Cu}} = 1000m_e$, and the mass of CH ions m_{CH}

and He ions m_{He} are calculated proportionally, which gives $f_m \sim 0.0085$. The parameters of number density $f_n = 10$ and temperature $f_T = 5$. These parameters lead to $t_1/t_0 \sim 0.0012$, i.e., 1.2 ps in PIC simulations represents 1.0 ns in RMHD simulations and experiments. In the PIC simulations, the ion charge state Z is always consistent with the RMHD simulations. The whole simulation box is divided into 1600×2400 grids, and 100 macro-particles per species are employed in each grid. To verify the convergence of the simulation, doubling the number of particles give identical results to the images shown. Open boundary conditions are also applied in each direction, and other set of transformation parameters hardly affect the final results.

Although the introduction of collision effects will destroy the self-consistency of similar transformations (due to the bad-scaled transport coefficient ν , η and χ), as long as the dimensionless parameters Re , R_m and Pe are far greater than 1.0, then this deviation is negligible. In the hybrid collisional-collisionless magnetic reconnection, the collision effect of Cu plasma may be important near the current sheet, where $\lambda_{ei} \sim 2\delta$. The commonly used parameter to evaluate the strength of the collision effect is L/λ_{ei} . In the PIC simulation, we keep this parameter consistent with the RMHD simulation and experiments. Because of $\lambda_{ei} \propto T_e^2/n_e$, the transformation parameter of the collision frequency is $\nu_{ei,1}/\nu_{ei,0} = f_T^2/\sqrt{f_m f_n}$. By this way, the binary Coulomb collision⁴⁶ can be appropriately included.

Synthetic proton radiography simulation. In order to directly compare with the experimental proton radiography images, we perform synthetic, numerical proton radiography simulation based on the magnetic fields obtained from the self-consistent combined RMHD-PIC simulation. The main steps are as follows: protons with a point source are magnified by point projection, then enter the area filled with magnetic fields and deflect by the Lorentz force. After escaping these magnetic fields, they perform a uniform linear motion and are finally deposited in the simulated RCF stacks. These protons are regarded as PIC macro-particles, and their energy is consistent with the experiments. The geometry and magnification rate of the system are also consistent with the experiments. The deflection motion of these protons in the magnetic fields adopts the Boris algorithm, and the magnetic field fluxes are equivalent to the path-integrated magnetic field ψ that extracted from the experimental images. These protons deposit energy in the simulated RCF stacks and gradually slow down until they stop. The stopping power of different materials come from the NIST Standard Reference Database⁵⁴, and the scattering effect is ignored. The accuracy of this code has been well benchmarked.

Data availability

All data that support the findings of this study are available from the corresponding author upon reasonable request.

Code availability

The FLASH Code is a radiation MHD simulation code for plasma physics and astrophysics, was developed in part by the DOE NNSA- and DOE Office of Science supported Flash Center for Computational Science at the University of Chicago and the University of Rochester. The code is available for download from <https://flash.rochester.edu/site/flashcode>. EPOCH is the Extendable PIC Open Collaboration project to develop a UK community advance relativistic EM PIC code. The open source code is available for download from <https://cfsa-pmw.warwick.ac.uk/EPOCH/epoch>. PROBLEM solver is an open source Python implementation of the proton radiography reconstruction algorithm of Bott (2017), the source code is available for download from <https://github.com/flash-center/PROBLEM>. The synthetic proton radiography simulation code are available from the corresponding author upon reasonable request.

Received: 17 April 2022; Accepted: 23 September 2022;

Published online: 08 October 2022

References

- Zweibel, E. G. & Yamada, M. Magnetic Reconnection in Astrophysical and Laboratory Plasmas. *Annu. Rev. Astron. Astrophys.* **47**, 291–332 (2009).
- Yamada, M., Kulsrud, R. & Ji, H. Magnetic reconnection. *Rev. Mod. Phys.* **82**, 603–664 (2010).
- Schrijver, C. J. et al. Large-scale coronal heating by the small-scale magnetic field of the Sun. *Nature* **394**, 152–154 (1998).
- Biskamp, D. Collisional and collisionless magnetic reconnection. *Phys. Plasmas* **4**, 1964–1968 (1997).
- Shibata, K. Chromospheric Anemone Jets as Evidence of Ubiquitous Reconnection. *Science* **318**, 1591–1595 (2007).
- Sweet, P. A. The Production of High Energy Particles in Solar Flares. *Nuovo Cim.* **8**, 188–196 (1958).

7. Parker, E. N. The solar flare phenomenon and the theory of reconnection and annihilation of magnetic fields. *Astrophys. J. Suppl. Ser.* **8**, 177–211 (1963).
8. Cassak, P. A. & Fuselier, S. A. Reconnection at Earth's Dayside Magnetopause. in *Magnetic Reconnection: Concepts and Applications* (eds. Gonzalez, W. & Parker, E.) 213–276 (Springer International Publishing, 2016).
9. Petrukovich, A., Artemyev, A. & Nakamura, R. Magnetotail Reconnection. in *Magnetic Reconnection: Concepts and Applications* (eds. Gonzalez, W. & Parker, E.) 277–313 (Springer International Publishing, 2016).
10. Hesse, M., Birn, J. & Kuznetsova, M. Collisionless magnetic reconnection: Electron processes and transport modeling. *J. Geophys. Res. Sp. Phys.* **106**, 3721–3735 (2001).
11. Hesse, M., Neukirch, T., Schindler, K., Kuznetsova, M. & Zenitani, S. The Diffusion Region in Collisionless Magnetic Reconnection. *Space Sci. Rev.* **160**, 3–23 (2011).
12. Yang, B. & Chen, H. Filament Eruption and Its Reformation Caused by Emerging Magnetic Flux. *Astrophys. J.* **874**, 96 (2019).
13. Li, L. et al. Magnetic reconnection between a solar filament and nearby coronal loops. *Nat. Phys.* **12**, 847–851 (2016).
14. Nilson, P. M. et al. Magnetic reconnection and plasma dynamics in two-beam laser-solid interactions. *Phys. Rev. Lett.* **97**, 255001 (2006).
15. Li, C. K. et al. Observation of megagauss-field topology changes due to magnetic reconnection in laser-produced plasmas. *Phys. Rev. Lett.* **99**, 055001 (2007).
16. Zhong, J. et al. Modelling loop-top X-ray source and reconnection outflows in solar flares with intense lasers. *Nat. Phys.* **6**, 984–987 (2010).
17. Fiksel, G. et al. Magnetic reconnection between colliding magnetized laser-produced plasma plumes. *Phys. Rev. Lett.* **113**, 105003 (2014).
18. Pei, X. X. et al. Magnetic reconnection driven by Gekko XII lasers with a Helmholtz capacitor-coil target. *Phys. Plasmas* **23**, 032125 (2016).
19. Law, K. F. F. et al. Relativistic magnetic reconnection in laser laboratory for testing an emission mechanism of hard-state black hole system. *Phys. Rev. E* **102**, 033202 (2020).
20. Kuramitsu, Y. et al. Magnetic reconnection driven by electron dynamics. *Nat. Commun.* **9**, 5109 (2018).
21. Rosenberg, M. J. et al. Slowing of Magnetic Reconnection Concurrent with Weakening Plasma Inflows and Increasing Collisionality in Strongly Driven Laser-Plasma Experiments. *Phys. Rev. Lett.* **114**, 205004 (2015).
22. Rosenberg, M. J. et al. A laboratory study of asymmetric magnetic reconnection in strongly driven plasmas. *Nat. Commun.* **6**, 6190 (2015).
23. Daughton, W. et al. Transition from collisional to kinetic regimes in large-scale reconnection layers. *Phys. Rev. Lett.* **103**, 065004 (2009).
24. Stanier, A. et al. Influence of 3D plasmoid dynamics on the transition from collisional to kinetic reconnection. *Phys. Plasmas* **26**, 072121 (2019).
25. Shibata, K. & Tanuma, S. Plasmoid-induced-reconnection and fractal reconnection. *Earth Sp. Sci.* **53**, 473–482 (2001).
26. Shibata, K. & Takasao, S. Fractal Reconnection in Solar and Stellar Environments. in *Magnetic Reconnection: Concepts and Applications* (eds. Gonzalez, W. & Parker, E.) 373–407 (Springer International Publishing, 2016).
27. Uzdensky, D. A. & Loureiro, N. F. Magnetic Reconnection Onset via Disruption of a Forming Current Sheet by the Tearing Instability. *Phys. Rev. Lett.* **116**, 105003 (2016).
28. Samtaney, R. et al. Formation of plasmoid chains in magnetic reconnection. *Phys. Rev. Lett.* **103**, 105004 (2009).
29. Uzdensky, D. A., Loureiro, N. F. & Schekochihin, A. A. Fast magnetic reconnection in the plasmoid-dominated regime. *Phys. Rev. Lett.* **105**, 235002 (2010).
30. Dong, Q.-L. et al. Plasmoid Ejection and Secondary Current Sheet Generation from Magnetic Reconnection in Laser-Plasma Interaction. *Phys. Rev. Lett.* **108**, 215001 (2012).
31. Hare, J. D. et al. Anomalous Heating and Plasmoid Formation in a Driven Magnetic Reconnection Experiment. *Phys. Rev. Lett.* **118**, 085001 (2017).
32. Petrasso, R. D. et al. Lorentz mapping of magnetic fields in hot dense plasmas. *Phys. Rev. Lett.* **103**, 085001 (2009).
33. Gao, L. et al. Precision mapping of laser-driven magnetic fields and their evolution in high-energy-density plasmas. *Phys. Rev. Lett.* **114**, 215003 (2015).
34. Bott, A. F. A. et al. Proton imaging of stochastic magnetic fields. *J. Plasma Phys.* **83**, 905830614 (2017).
35. Graziani, C., Tzeferacos, P., Lamb, D. Q. & Li, C. Inferring morphology and strength of magnetic fields from proton radiographs. *Rev. Sci. Instrum.* **88**, 123507 (2017).
36. Tubman, E. R. et al. Observations of pressure anisotropy effects within semi-collisional magnetized plasma bubbles. *Nat. Commun.* **12**, 334 (2021).
37. Fryxell, B. et al. FLASH : An Adaptive Mesh Hydrodynamics Code for Modeling Astrophysical Thermonuclear Flashes. *Astrophysical J. Suppl. Ser.* **131**, 273–334 (2000).
38. Heltemes, T. A. & Moses, G. A. BADGER v1.0: A Fortran equation of state library. *Comput. Phys. Commun.* **183**, 2629–2646 (2012).
39. Macfarlane, J. J. IONMIX—a code for computing the equation of state and radiative properties of LTE and non-LTE plasmas. *Comput. Phys. Commun.* **56**, 259–278 (1989).
40. Fox, W., Bhattacharjee, A. & Germaschewski, K. Fast Magnetic Reconnection in Laser-Produced Plasma Bubbles. *Phys. Rev. Lett.* **106**, 215003 (2011).
41. Totorica, S. R., Abel, T. & Fiuza, F. Nonthermal Electron Energization from Magnetic Reconnection in Laser-Driven Plasmas. *Phys. Rev. Lett.* **116**, 095003 (2016).
42. Xu, Z. et al. Characterization of magnetic reconnection in the high-energy-density regime. *Phys. Rev. E* **93**, 033206 (2016).
43. Remington, B. A., Arnett, D., Drake, R. P. & Takabe, H. Modeling Astrophysical Phenomena in the Laboratory with Intense Lasers. *Science* **284**, 1488–1493 (1999).
44. Ryutov, D. D., Drake, R. P. & Remington, B. A. Criteria for Scaled Laboratory Simulations of Astrophysical MHD Phenomena. *Astrophys. J. Suppl. Ser.* **127**, 465–468 (2000).
45. Ryutov, D. D., Remington, B. A., Robey, H. F., Drake, R. P. & Introduction, I. Magnetohydrodynamic scaling: From astrophysics to the laboratory*. *Phys. Plasmas* **8**, 1804 (2001).
46. Nambu, K. & Yonemura, S. Weighted Particles in Coulomb Collision Simulations Based on the Theory of a Cumulative Scattering Angle. *J. Comput. Phys.* **145**, 639–654 (1998).
47. Arber, T. D. et al. Contemporary particle-in-cell approach to laser-plasma modelling. *Plasma Phys. Controlled. Fusion* **57**, 113001 (2015).
48. Comisso, L. et al. General theory of the plasmoid instability. *Phys. Plasmas* **23**, 100702 (2016).
49. Comisso, L. et al. Plasmoid Instability in Forming Current Sheets. *Astrophys. J.* **850**, 142 (2017).
50. Fitzpatrick, R. Collisionless magnetic reconnection with arbitrary guide field. *Phys. Plasmas* **11**, 4713 (2004).
51. Loureiro, N. F. & Boldyrev, S. Collisionless Reconnection in Magnetohydrodynamic and Kinetic Turbulence. *Astrophys. J.* **850**, 182 (2017).
52. Hosseinpour, M. A fast tearing mode instability driven by agyrotropic electron pressure. *Adv. Sp. Res.* **54**, 955–960 (2014).
53. Guo, L.-J. et al. Observations and Modeling of the Onset of Fast Reconnection in the Solar Transition Region. *Astrophys. J.* **901**, 148 (2020).
54. NIST Standard Reference Database, <https://www.nist.gov/pml/stopping-power-range-tables-electrons-protons-and-helium-ions>, (2017).

Acknowledgements

This work is supported by National Natural Science Foundation of China, Grant Nos. 12135001, 11825502 and 11921006; Science Challenge Project, No. TZ2018005; the Strategic Priority Research Program of Chinese Academy of Sciences, Grant No. XDA25050900; Bin Qiao acknowledges supports from National Natural Science Funds for Distinguished Young Scholar, Grant No. 11825502 and the Joint Laboratory on High Power Laser and Physics, Shanghai Institute of Optics and Fine Mechanics. The simulations are carried out on the Tianhe-2 supercomputer at the National Supercomputer Center in Guangzhou.

Author contributions

Bin Qiao and Shaoping Zhu proposed and were in charge of the research campaign as principle investigators. Zhonghai Zhao, Yu Xie, Zhu Lei, Weipeng Yao, Wenqiang Yuan and Bin Qiao carried the simulations, the data analysis. Honghai An, Zhonghai Zhao, Jun Xiong, Chen Wang, Junjian Ye, Zhiyong Xie, Zhiheng Fang, Anle Lei, Wei Wang, Weimin Zhou and Bin Qiao carried out the experiments. Bin Qiao and Zhonghai Zhao wrote the paper. Wenbing Pei, Shaoping Zhu and Xiantu He contributed to theoretical interpretations of the results.

Competing interests

The authors declare no competing interests.

Additional information

Supplementary information The online version contains supplementary material available at <https://doi.org/10.1038/s42005-022-01026-7>.

Correspondence and requests for materials should be addressed to Weimin Zhou, Wei Wang, Shaoping Zhu or Bin Qiao.

Peer review information *Communications Physics* thanks Luca Comisso, Shinsuke Fujioka and the other, anonymous, reviewer(s) for their contribution to the peer review of this work. Peer reviewer reports are available.

Reprints and permission information is available at <http://www.nature.com/reprints>

Publisher's note Springer Nature remains neutral with regard to jurisdictional claims in published maps and institutional affiliations.



Open Access This article is licensed under a Creative Commons Attribution 4.0 International License, which permits use, sharing, adaptation, distribution and reproduction in any medium or format, as long as you give appropriate credit to the original author(s) and the source, provide a link to the Creative Commons license, and indicate if changes were made. The images or other third party material in this article are included in the article's Creative Commons license, unless indicated otherwise in a credit line to the material. If material is not included in the article's Creative Commons license and your intended use is not permitted by statutory regulation or exceeds the permitted use, you will need to obtain permission directly from the copyright holder. To view a copy of this license, visit <http://creativecommons.org/licenses/by/4.0/>.

© The Author(s) 2022